High-Temperature Carbon Dioxide Capture in a Porous Material via Reversible Metal–Ligand Insertion

Authors: Rachel C. Rohde[1†], Kurtis M. Carsch[1†], Matthew N. Dods[3], Henry Z. H. Jiang[1], Alexandra McIsaac[1,2], Ryan A. Klein[4,5], Hyunchul Kwon[1], Sarah L. Karstens[1], Yang Wang[1], Kaitlyn E. Engler[3], Adrian J. Huang[1], Jordan W. Taylor[1], Yuto Yabuuchi[1], Jeffrey A. Reimer[2,3], Martin Head-Gordon[1,2], Craig M. Brown[4,5], Jeffrey R. Long[1,2,3]*

Affiliations:

[1]Department of Chemistry, University of California, Berkeley, CA 94720, USA.
[2]Materials Sciences Division, Lawrence Berkeley National Laboratory, Berkeley, CA 94720, USA.
[3]Department of Chemical and Biomolecular Engineering, University of California, Berkeley, CA 94720, USA.
[4]Center for Neutron Research, National Institute of Standards and Technology, Gaithersburg, MD 20899, USA.
[5]Chemical and Biomolecular Engineering, University of Delaware, Newark, DE 19716, USA.

*Corresponding author. Email: jrlong@berkeley.edu

[†]These authors contributed equally to this work.

Abstract. Carbon capture is an attractive strategy to mitigate point-source CO_2 emissions, but there remain substantial hurdles to widespread adoption of state-of-the-art aqueous amine technologies. The capture of CO_2 at temperatures closer to those of many industrial flue streams (>200 °C) has attracted significant interest, although candidate sorbents typically exhibit low CO_2 capacities and poor stability to extended cycling. Here, we report a metal–organic framework that reversibly chemisorbs CO_2 at temperatures between 200 and 400 °C that are unprecedented for an intrinsically porous material. Gas sorption, structural, and spectroscopic analyses confirm the rapid, reversible nature of this transformation, which is kinetically limited at ambient temperatures. The material is robust to isothermal adsorption–desorption cycling under conditions relevant to carbon capture from various industrial flue gases.

One Sentence Summary. A metal–organic framework featuring terminal Zn–H sites reversibly captures CO_2 at temperatures between 200 and 400 °C.

The widespread implementation of carbon capture technology is an essential strategy to limit global warming (*1*, *2*) and is slated to have the greatest impact in the energy generation and industrial sectors, which together account for more than two-thirds of global CO_2 emissions. Although the use of renewable sources is accelerating (*3*), fossil fuels are projected to supply the majority of the world's power in the next few decades (*4*). In the industrial sector, some of the most carbon-intensive industrial processes—such as steel and cement making—are difficult to fully integrate with a renewable electrical grid and produce unavoidable CO_2 as an inherent byproduct of the underlying chemical processes (*5,* 6). The most advanced CO_2 capture technology is post-combustion capture using aqueous amine solutions (*7*), which react with CO_2 at moderate temperatures (~40 to 60 °C) to form soluble carbamates (*8*). However, the high regeneration energies, corrosive degradation products, and volatility of these solutions (*9*) have thus far

precluded their adoption at large scales. The widespread use of alkanolamines would also require cooling of effluent streams from most point sources, which is projected to add sizably to capital expenditures from thermal management and freshwater consumption (*10*, *11*).

Alternatively, the capture of CO_2 at higher temperatures closer to those of many exhaust streams would minimize or obviate the need for capitally intensive cooling and could facilitate the recuperation of quality heat generated upon exothermic CO_2 sorption (*12*, *13*) (see Section 1 of the Supplementary Materials [SM]). This prospect has motivated extensive research on metal oxides that react reversibly with CO_2 to form solid metal carbonates at high temperatures (~150 to 1200 °C) (*12*, *13*), and the established calcium looping process, which utilizing CaO, has been found to be competitive with monoethanolamine solutions for post-combustion CO_2 capture (*14–16*). However, metal oxides are prone to sintering and deactivation with repeated cycling and typically require large temperature swings for regeneration. Porous metal–organic frameworks (MOFs) have been developed more recently for CO_2 capture (*17*, 18), and amine-appended frameworks in particular boast large CO_2 working capacities, low regeneration energies, and exceptional stability to long-term cycling (*18–23*). However, MOFs typically capture appreciable CO_2 only at temperatures well below 150 °C.

Both the metal oxides and amine-appended MOFs capture CO_2 via reversible chemisorption mechanisms involving the reaction of CO_2 with a nucleophilic ligand. Another example of such reactivity is CO_2 insertion into terminal zinc–hydride bonds in molecular compounds, resulting in zinc–formate species (*24–28*). In zinc–hydride complexes supported with tris(pyrazolyl)borate ligands, this reactivity occurs at ~50 °C over the course of several days (*23*, *27*), suggesting that despite the thermodynamically favored formation of strong C–H bonds, there is a kinetic barrier to CO_2 insertion. Interestingly, the reverse reaction has been demonstrated for the framework $Zn_5(OOCH)_xCl_{4-x}(btdd)_3$ (Zn(OOCH)-MFU-4*l*; H_2btdd = bis(1*H*-1,2,3-triazolo[4,5-*b*],[4′,5′-*i*])dibenzo[1,4]dioxin; MFU-4*l* = $Zn_5Cl_4(btdd)_3$), which evolves CO_2 at temperatures above 200 °C to form ZnH-MFU-4*l* ($Zn_5H_xCl_{4-x}(btdd)_3$) (*29*). The pseudo-tetrahedral Zn^{II} sites in both frameworks exhibit a coordination environment akin to that in tris(pyrazolyl)borate supported complexes.

Here, we disclose that ZnH-MFU-4*l* (Fig. 1A) reversibly captures CO_2 to form Zn(OOCH)-MFU-4*l* in a manner akin to molecular zinc–hydride compounds, via an insertion mechanism that occurs only at temperatures above 100 °C and becomes reversible at temperatures ranging from 200 to 400 °C (Fig. 1B). The zinc–hydride/zinc–formate interconversion mechanism is confirmed using x-ray diffraction analysis, multinuclear nuclear magnetic resonance (NMR) spectroscopy, and *in situ* diffuse reflectance infrared Fourier transform spectroscopy (DRIFTS). The framework is robust to repeated isothermal adsorption–desorption cycling, and its rapid CO_2 sorption kinetics enable the capture of large quantities of CO_2 under conditions relevant to cement and steel manufacturing exhaust streams. These results demonstrate for the first time the applicability of porous materials for high-temperature CO_2 capture.

Synthesis and preliminary characterization

The framework ZnH-MFU-4*l* was previously prepared from MFU-4*l* (*30*) via formate exchange to generate Zn(OOCH)-MFU-4*l*, followed by thermolysis at 300 °C to drive off CO_2 (*29*). In our hands, this preparation yielded ZnH-MFU-4*l* with hydride estimated to occupy ~73% of the peripheral zinc(II) sites, determined from ^{1}H NMR spectroscopy analysis of a digested sample of the Zn(OOCH)-MFU-4*l* precursor (fig. S51). Seeking to optimize the zinc–hydride loading, we devised an alternative synthesis involving alkylation of MFU-4*l* with diethylzinc to access ZnEt-

MFU-4*l* (*31*), followed by protonolysis with formic acid to yield Zn(OOCH)-MFU-4*l*. Heating the zinc–formate framework under dynamic vacuum or N_2 afforded ZnH-MFU-4*l* as an off-white, microcrystalline powder. Energy-dispersive x-ray (EDX) spectroscopy analysis revealed a small fraction (6%) of the zinc(II) sites remain coordinated by chloride (fig. S41). Correspondingly, analysis of N_2 adsorption data obtained at 77 K revealed a higher Brunauer–Emmett–Teller surface area of 3920(70) m^2/g (fig. S2) than that reported previously, while the infrared spectrum remains consistent with literature values, featuring a diagnostic Zn–H vibration at 1792 cm^{-1} (*29*) (ν(Zn–D) = 1289 cm^{-1}, c.f. 1277 cm^{-1} for a simple harmonic oscillator, fig. S56) . Of note, we also devised an alternative synthesis of ZnH-MFU-4*l* that can be performed in air without the exclusion water (see section 3.8 of the SM for details). However, the number of hydride sites in ZnH-MFU-4*l* prepared via this approach are slightly lower ($Zn_5H_{3.5}Br_{0.5}(btdd)_3$ based on ^1H NMR spectroscopy, fig. S44), because of this, all subsequent analyses were carried out using material prepared via the alkylation and protonolysis route.

Through a series of single-crystal-to-single-crystal transformations starting from ZnEt-MFU-4*l*, it was possible to isolate crystals of ZnH-MFU-4*l* suitable for x-ray diffraction analysis (Fig. 1B; see section 3.11 of the SM). The terminal hydride ligand was located in the Fourier difference map, and the electron density data refined to yield a Zn–H bond length of 1.67(1) Å, which is within the range of reported Zn–H distances for various molecular compounds (*27*). While the stability of ZnH-MFU-4*l* to atmosphere and moisture was not previously reported, we found it to be robust in air at ambient temperature for at least 18 months, based on powder x-ray diffraction and infrared spectroscopy analyses (figs. S58 and S67). Thermogravimetric analysis (TGA) data collected for ZnH-MFU-4*l* under pure N_2 revealed that the framework is also thermally robust and is stable up to approximately 450 °C (fig. S21). In contrast, decarboxylation of Zn(OOCH)-MFU-4*l* to give ZnH-MFU-4*l* occurs above 180 °C (*29*).

Interestingly, TGA data collected for Zn(OOCH)-MFU-4*l* under an atmosphere of pure CO_2 revealed only a gradual decline in sample mass up to 300 °C, indicating carboxylation is suppressed under these conditions (Fig. 2A). In contrast, the thermal ramp profile of ZnH-MFU-4*l* under CO_2 is unusual and features an initial small mass increase followed by a near plateau until about 50 °C, after which point the mass increases until 100 °C and holds relatively constant up to 300 °C. The profile for ZnH-MFU-4*l* also mirrors that of Zn(OOCH)-MFU-4*l* above 100 °C, suggesting that the mass increase observed for ZnH-MFU-4*l* at elevated temperatures is associated with CO_2 insertion into the Zn–H units to yield Zn(OOCH)-MFU-4*l*. Data collected for ZnH-MFU-4*l* under an atmosphere of only 20% CO_2 in N_2 feature a similar profile (fig. S22).

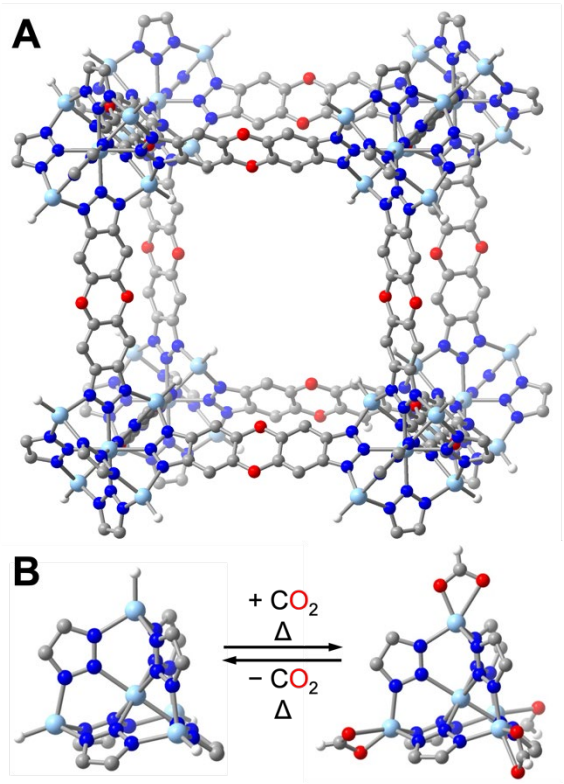

Fig. 1. Reversible high-temperature CO_2 chemisorption in a zinc–hydride MOF. (**A**) Illustration of a portion of the structure of ZnH-MFU-4*l* as determined from single-crystal x-ray diffraction analysis in the present work. (**B**) Expanded view of a cluster node of the framework ($d_{Zn–H}$ = 1.67(1) Å). At temperatures above 200 °C, CO_2 reversibly inserts into the Zn–H bonds of ZnH-MFU-4*l* to generate Zn–formate species. Light blue, gray, blue, red, and white spheres represent Zn, C, N, O, and H atoms, respectively.

CO_2 Adsorption Properties and Isothermal Operation at Elevated Temperatures

Single-component CO_2 adsorption isotherms were collected at 25, 150, 200, 250, and 300 °C to further investigate the temperature-dependent CO_2 adsorption properties of ZnH-MFU-4*l* (Fig. 2B). At 25 °C, CO_2 uptake is very gradual, and the material achieves a capacity of 1.16 mmol/g at 1 bar. In contrast, the high-temperature CO_2 adsorption data are characterized by steep uptake in the low-pressure region, indicative of strong CO_2–framework interactions. For example, at 150 °C the material achieved a capacity of 3.27 mmol/g at only 10 mbar, in excellent agreement with the predicted capacity of 3.3 mmol/g if one molecule of CO_2 were to bind at each of the zinc–hydride sites. At higher pressures, the uptake begins to plateau, reaching a value of 3.52 mmol/g at 1 bar. Steep CO_2 uptake also occurs at 200, 250, and 300 °C, and at these temperatures, the material achieves a capacity of 3.27 mmol/g at pressures of 65, 200, and 600 mbar, respectively. At these higher temperatures, CO_2 can also be fully desorbed without hysteresis using only vacuum.

A dual-site Langmuir-Freundlich model was used to fit CO_2 adsorption isotherms for ZnH-MFU-4*l* at 280, 290, and 300 °C (see fig. S10 and table S4) and the corresponding simultaneous fit parameters were used with the Clausius–Clapeyron equation to determine the isosteric enthalpy (ΔH_{ads}) of CO_2 adsorption as a function of loading (fig. S17). At low loadings, ΔH_{ads} = −93(1) kJ/mol and remains relatively constant up to a loading of ~2.7 mmol/g, consistent with strong CO_2

chemisorption at the isolated Zn–H sites in ZnH-MFU-4*l*. This CO_2 adsorption enthalpy value is among the highest values reported to date for MOFs (*19*, *21*, *32*).

At CO_2 concentrations and temperatures relevant to emissions from iron and steelmaking (e.g., blast furnace exhaust with 21% CO_2 at 300 °C) (*33*) and the cement industry (300 °C exhaust stream with 30% CO_2) (*34*), ZnH-MFU-4*l* exhibits high capacities of 3.06 and 3.15 mmol/g. Importantly, single-component CH_4, N_2, H_2, C_2H_4, C_2H_6, and CO adsorption isotherms collected for ZnH-MFU-4*l* at 300 °C and pressures up to 1 bar revealed negligible uptake of these other industrially relevant gases, indicating that the framework is highly selective for CO_2 (fig. S12). Ultimately, the high-temperature CO_2 adsorption behavior exhibited by ZnH-MFU-4*l* is unprecedented among porous materials such as MOFs and zeolites, which typically exhibit decreasing CO_2 capacities with increasing temperature. As a result, there is limited CO_2 uptake data reported for porous adsorbents above 100 °C, although the measured capacity of 3.47 mmol/g for ZnH-MFU-4*l* at 200 °C and 1 bar far exceeds reported capacities for Mg_2(dobdc) (dobdc^{4-} = 1,4-dioxido-2,5-benzenedicarboxylate; Mg-MOF-74) and zeolite 13X under the same conditions, 0.85 and 0.54 mmol/g, respectively (*35*, *36*).

Of note, ZnH-MFU-4*l* is only one member of a potentially large family of frameworks featuring zinc–hydride sites capable of high-temperature CO_2 capture. Indeed, starting from the related material CFA-1 ($Zn_5(OAc)_4(bibta)_3$; H_2bibta = 1*H*,1′*H*-5,5′-bibenzo[*d*][1,2,3]triazole) (*37*), which features the flexible and less costly (*38*) bibta^{2-} linker in place of btdd^{2-}, we prepared ZnH-CFA-1 (see section 3.14 of the SM). Analogous to ZnH-MFU-4*l*, this framework also captures CO_2 reversibly at 250 °C (fig. S16). Our preliminary analysis of this material suggests it is not as thermally stable as ZnH-MFU-4*l* at temperatures above 250 °C (fig. S29); however, research is ongoing in our laboratory on ZnH-CFA-1 and related materials.

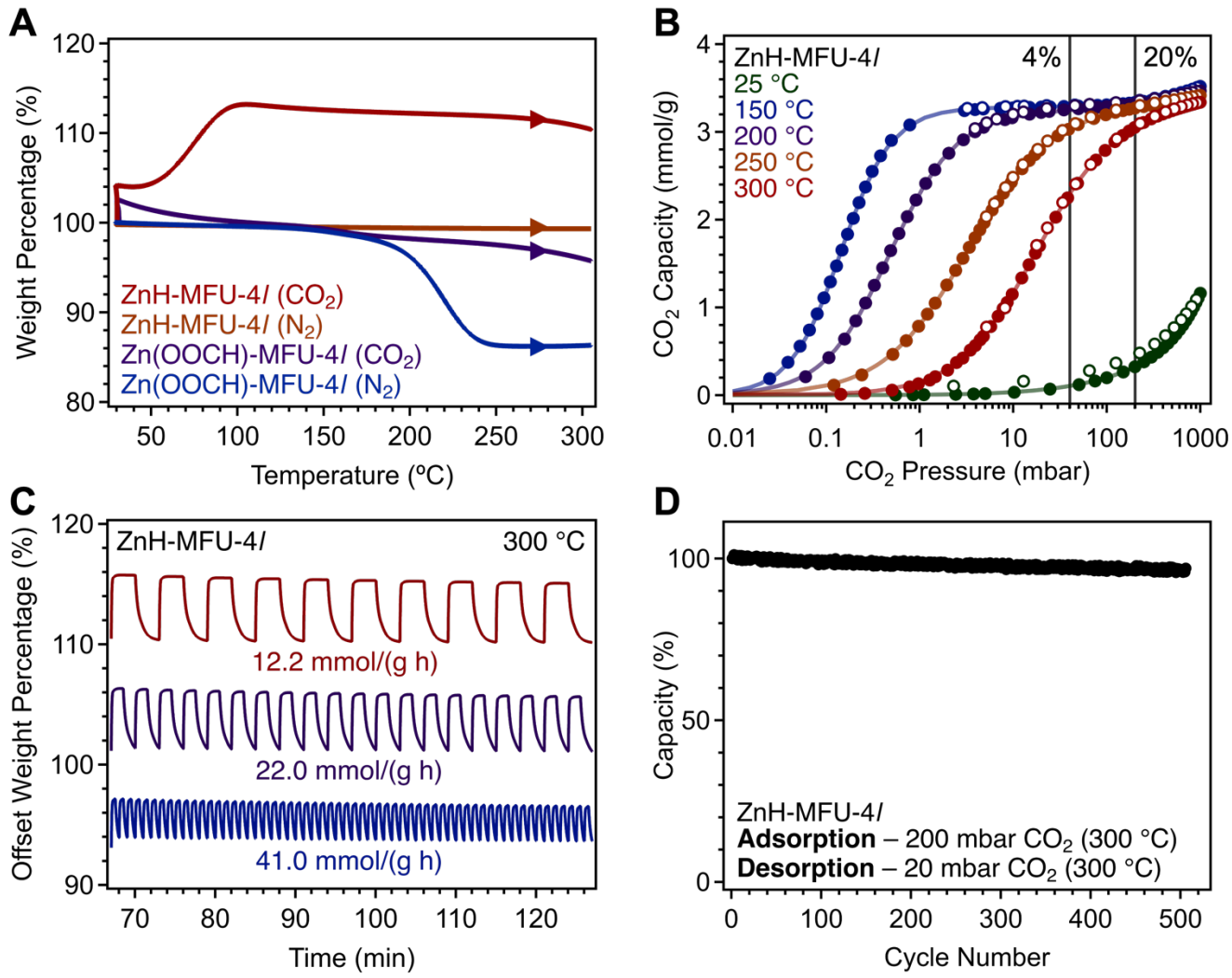

Fig. 2. High-temperature isobaric and isothermal CO_2 adsorption data for ZnH-MFU-4*l*. (**A**) Thermogravimetric analysis data collected for ZnH-MFU-4*l* and Zn(OOCH)-MFU-4*l* under an atmosphere of pure CO_2 or N_2. (**B**) Variable-temperature CO_2 adsorption (filled circles) and desorption (empty circles) isotherms for ZnH-MFU-4*l*. Solid lines are guides for the eyes. Vertical lines denote CO_2 concentrations relevant to flue streams produced from natural gas combustion (4% CO_2) and cement and steelmaking (20% CO_2 and higher) (*18*, *33, 34*). (**C**) Adsorption (200 mbar CO_2 in N_2) and desorption (15 mbar CO_2 in N_2) cycling data collected for ZnH-MFU-4*l* at 300 °C with adsorption (and desorption) times of 0.5, 1.5, or 3 minutes (magenta, blue, and purple traces, respectively). Capacities achieved after the first cycle were 0.69 mmol/g (1-min cycles), 1.13 (1.5-min cycles), and 1.21 mmol/g (3-min cycles), and after 10, 20, and 60 cycles, and after the final cycles, the capacities were 0.64 mmol/g, 1.06 mmol/g, and 1.14 mmol/g, respectively. The CO_2 "capture throughputs" achieved in each case are indicated. (**D**) Cycling data for ZnH-MFU-4*l* over the course of 508 isothermal adsorption (200 mbar CO_2) and desorption (20 mbar CO_2) cycles at 300 °C, plotted as a percentage of the capacity measured for the first cycle (1.24 mmol/g).

Adsorption–desorption cycling performance under diverse conditions

To investigate high-temperature CO_2 capture performance of ZnH-MFU-4*l* under realistic conditions, we carried out isothermal cycling experiments at 300 °C on a TGA with adsorption occurring under flowing streams of 20% CO_2 in N_2 and desorption affected by flowing 1.5% CO_2 in N_2, simulating capture from cement flue gas with industrial-grade vacuum regeneration with selected matched adsorption and desorption times of 0.5, 1.5 or 3 minutes (Fig. 3C). In all cases, ZnH-MFU-4*l* exhibited excellent stability to repeated cycling and retained >92% of its initial capacity after the final cycle after 1 h. Note, while longer cycle times would be associated with capacities approaching the equilibrium capacity of the material, we selected these shorter cycle times to highlight that large CO_2 "capture throughputs"—defined here as mmol CO_2 captured per gram ZnH-MFU-4*l* per hour (mmol/(g·h))—can be achieved with relatively short cycle times. For example, the capture throughput when using 60-second cycles was 41.0 mmol/(g·h), more than three times the throughput 12.2 mmol/(g·h) achieved with 360-s cycles (Fig. 2C). These results highlight the rapid kinetics of CO_2 adsorption and desorption in ZnH-MFU-4*l* (discussed further below). Additionally, unlike most metal oxides, ZnH-MFU-4*l* can be isothermally regenerated and does not require energy-intensive temperature swings for regeneration. Another interesting result from these experiments is the demonstration that high capture capacities and throughputs can be achieved using matched adsorption and desorption times. As a result, in a practical separation process, it may be possible to vastly simplify adsorber scheduling by employing only two beds in parallel, for example, one adsorbing and one desorbing at any time.

Isothermal cycling data were also collected for ZnH-MFU-4*l* at 300 °C under conditions designed to simulate equilibrium CO_2 capture from cement flue gas (adsorption: 200 mbar CO_2) and regeneration under simulated industrial vacuum (desorption: 20 mbar CO_2, see fig. S20 for details) (*39*, *40*). The material exhibited exceptional stability to long-term cycling under these conditions. Indeed, after 508 cycles, ZnH-MFU-4*l* retained greater than 96% of its initial adsorption capacity (1.24 mmol/g) (Fig. 2D). Further, preliminary TGA cycling data collected at 400 °C (adsorption: 20% CO_2 in N_2; desorption under pure N_2; see fig. S25) and under more oxidizing conditions (adsorption: 4% O_2, 15% CO_2, 81% N_2 at 300 °C; desorption under pure N_2 at 300 °C; see fig. S27) suggest that the material is robust under these more extreme conditions. Finally, preliminary IR spectroscopy data indicate that CO_2 insertion in ZnH-MFU-4*l* to form Zn(OOCH)-MFU-4*l* is favored at high temperature even in the presence of water vapor (fig. S62), an essential property as water vapor is a prevalent component of many CO_2 emissions streams (*18*). Investigation of the high-temperature CO_2 capture properties of ZnH-MFU-4*l* under more complex mixed-gas and humid streams is ongoing in our laboratory.

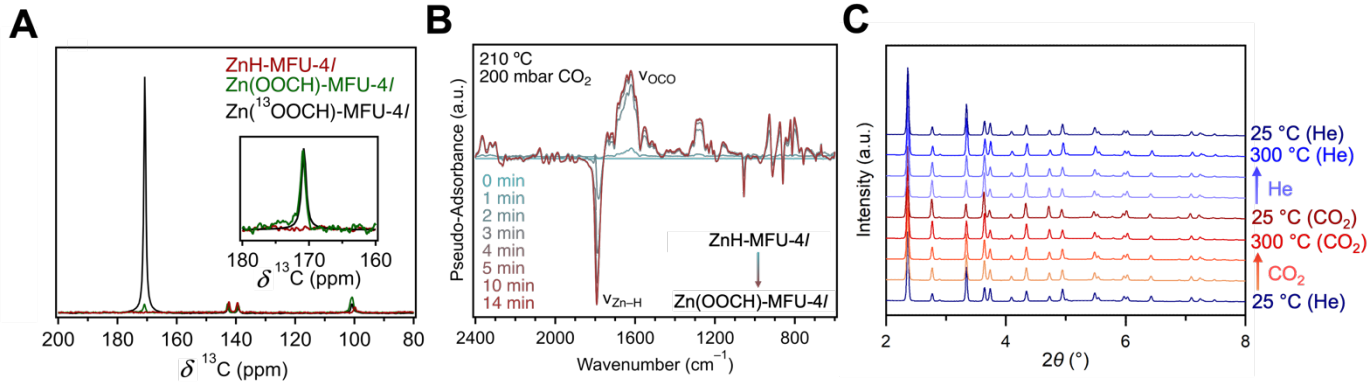

Fig. 3. Spectroscopic and structural characterization of reversible CO_2 chemisorption in ZnH-MFU-4*l*. (**A**) Solid-state ^{13}C NMR spectra for ZnH-MFU-4*l*, Zn(OOCH)-MFU-4*l*, and ZnH-

MFU-4*l* dosed with 1 bar $^{13}CO_2$ at ~280 °C, revealing a clear peak at 170.8 ppm corresponding to formate in Zn(OOCH)-MFU-4*l* and Zn(OO^{13}CH)-MFU-4*l*. The inset depicts the intensity-normalized formate ^{13}C resonance. (**B**) Difference spectra obtained from subtracting time-resolved DRIFTS data for a sample of ZnH-MFU-4*l* dosed *in situ* with 200 mbar CO_2 at 210 °C from a spectrum collected for ZnH-MFU-4*l* at 210 °C (t = 0 corresponds to immediately after dosing). (**C**) Starting from a sample of ZnH-MFU-4*l* cooled from 300 to 25 °C under He (bottom blue trace), *in situ* powder x-ray diffraction patterns (λ = 0.45207 Å) collected for ZnH-MFU-4*l* over the course of heating from 25 to 300 °C and then cooling under flowing CO_2 (10 sccm, light pink to dark red traces); heating from 25 to 300 °C under He to desorb CO_2; and finally cooling to 25 °C under He (10 sccm; blue traces). Comparison of the top and bottom patterns indicate that the structure of ZnH-MFU-4*l* is the same after cycling. Select patterns are shown to highlight changes with heating under the different gas atmospheres. More data are given in fig. S70, and experimental details are given in section 8.2 of the SM.

Structural and spectroscopic investigation of CO_2 adsorption mechanism

The mechanism of CO_2 adsorption in ZnH-MFU-4*l* was investigated using x-ray diffraction and solid-state NMR spectroscopy. Single-crystal x-ray diffraction analysis of crystals of ZnH-MFU-4*l* dosed with 200 mbar CO_2 at 200 °C for 10 min revealed conversion to Zn(OOCH)-MFU-4*l*, confirming that the CO_2 uptake in ZnH-MFU-4*l* occurs through insertion into the Zn–H bonds (Fig. 1B, fig. S79). Solid-state ^{13}C NMR spectra (with cross-polarization from ^{1}H) were collected for Zn(OOCH)-MFU-4*l*, ZnH-MFU-4*l*, and a sample of ZnH-MFU-4*l* dosed with ~1 bar $^{13}CO_2$ at 280 °C. Peaks at 100.9, 139.3, and 142.8 ppm in all three spectra were assigned to the btdd^{2-} linker, while a ^{13}C resonance at 170.8 ppm in the spectra for Zn(OOCH)-MFU-4*l* and Zn(OO^{13}CH)-MFU-4*l* was assigned to the carbon atom of the bound formate (Fig. 3A). In the solid-state ^{1}H NMR spectrum of Zn(OOCH)-MFU-4*l*, the formate C–H resonance is located at 8.9 ppm, and this feature is split into two resonances at 8.6 and a 9.1 ppm in Zn(OO^{13}CH)-MFU-4*l* (fig. S54), due to hyperfine coupling with ^{13}C, as support by ^{13}C{^{1}H}-HETCOR data (fig. S55).

In situ DRIFTS data collected for ZnH-MFU-4*l* further support the reversibility of the insertion mechanism. Time-resolved difference spectra were generated by subtracting the evolving spectra collected for the CO_2-dosed sample from the spectrum of ZnH-MFU-4*l* at 210 °C (Fig. 3B). With increasing time, a broad positive C=O vibration grows in at 1613 cm^{-1}, concomitant with growth of a negative Zn–H vibration at 1792 cm^{-1}, consistent with conversion of ZnH-MFU-4*l* to Zn(OOCH)-MFU-4*l*. *In situ* DRIFTS data were also collected for ZnH-MFU-4*l* under conditions designed to mimic an isothermal CO_2 adsorption–desorption cycle at 300 °C (see fig. S64). In brief, activated ZnH-MFU-4*l* was dosed with 200 mbar CO_2, which resulted in near complete disappearance of the $\nu_{Zn–H}$ feature at 1792 cm^{-1} (incomplete conversion to Zn(OOCH)-MFU-4*l* under these conditions is expected based on the single-component CO_2 isotherm data, see Fig. 2B). A final spectrum collected under N_2 following evacuation of the material revealed complete recovery of the $\nu_{Zn–H}$ feature, based on the integrated peak areas in the initial and final spectra.

Finally, *in situ* gas-dosed powder x-ray diffraction data were collected for a sample of ZnH-MFU-4*l* to examine structural changes occurring upon CO_2 adsorption and desorption at elevated temperatures (see section 8.2 of the SM for details of data collection and analysis). Starting from a sample of activated ZnH-MFU-4*l*, diffraction patterns were collected over the course of heating from 25 to 300 °C under flowing CO_2. Clear changes were apparent in the data upon increasing temperature starting at ~100 °C, with noticeable increases in the intensities of reflections at 2.36, 3.65, and 3.74 2θ (Fig. 3C and fig S71), which corresponded to an increase in lattice parameters

as determined from Pawley fits of the diffractograms (fig. S75). Rietveld refinement of the diffraction pattern collected at 300 °C under CO_2 yielded a structure model consistent with Zn(OOCH)-MFU-4*l* (Fig. 3D and figs. S71–S72). Following cooling to 25 °C under CO_2, the sample was heated to 300 °C under flowing He to regenerate ZnH-MFU-4*l*, and then finally cooled under He. Rietveld refinement of the diffraction patterns allowed for analysis of formate occupancy throughout the cycling, which supports the reversible interconversion of ZnH-MFU-4*l* and Zn(OOCH)-MFU-4*l* (fig. S74).

Investigation of Kinetics and Free Energy Landscape for CO_2 insertion

We investigated the kinetics of CO_2 adsorption in ZnH-MFU-4*l* from gas streams containing as little as 1.5% CO_2 in N_2 up to 100% CO_2 and at temperatures ranging from 160 to 300 °C (see Fig. 4A and figs. S34–S37). Higher CO_2 concentrations and higher temperatures resulted in more rapid adsorption kinetics and faster equilibration times (Fig. 4B). When exposed to a 20% CO_2 in N_2 stream at 300 °C, ZnH-MFU-4*l* achieves 90% of the equilibrium CO_2 capacity (3.12 mmol/g) within only nine seconds (Fig. 4A). This gravimetric capacity is similar to that determined from CO_2 isotherm measurements at 300 °C and 200 mbar CO_2 (3.05 mmol/g). Variable-temperature kinetic traces for CO_2 adsorption (20% CO_2 in N_2) and desorption (under N_2) were satisfactorily modelled with a first-order rate law (Fig. 4C and figs. S38–S40). Application of the Eyring equation yielded values for the entropy and enthalpy of activation of $\Delta H_{ads}^{\ddagger}$ = 54(4) kJ/mol and $\Delta S_{ads}^{\ddagger}$ = −130(4) J/(mol K), respectively at 298 K, revealing a significant entropic penalty associated with CO_2 activation. For the decarboxylation reaction, the activation enthalpy is very large, while the activation enthalpy is small ($\Delta H_{des}^{\ddagger}$ = 130(4) kJ/mol, $\Delta S_{des}^{\ddagger}$ = −21(4) J/(mol K) at 298 K).

Density functional theory (DFT) calculations carried out on the model cluster $Zn_5H_4(bta)_6$ (bta^- = benzotriazolate) yielded activation enthalpies and entropies for adsorption and desorption that are consistent with the experimental values ($\Delta H_{ads}^{\ddagger}$(calc) = 60 kJ/mol, $\Delta S_{ads}^{\ddagger}$(calc) = −116 J/(mol K) and $\Delta H_{des}^{\ddagger}$(calc) = 141 kJ/mol, $\Delta S_{des}^{\ddagger}$(calc) = 1.8 J/(mol K)) (see section 10 of the SM and table S17). Using the corresponding calculated activation energies for CO_2 adsorption at 298 and 548 K ($\Delta G_{ads,298K}^{\ddagger}$ = 95 kJ/mol, $\Delta G_{ads,548K}^{\ddagger}$ = 124 kJ/mol; see Fig. 5A) and the Eyring equation, we found that the rate constant for CO_2 insertion at 548 K is five orders of magnitude greater than at 298 K (see Section 6.4 in the Supplementary Materials), which serves to explain why CO_2 chemisorption occurs only at elevated temperatures. Interestingly, in the calculated transition state for CO_2 insertion, the hydride ligand comes into close contact with one of the benzotriazolate ligands, resulting in an unfavorable steric interaction that likely contributes to the large kinetic barrier (Fig 5B). Additionally, the calculated $\Delta G_{548K}^{\ddagger}$ for desorption is very close to $\Delta G_{548K}^{\ddagger}$ for adsorption (~140 versus ~124 kJ/mol), suggesting that, as discussed above, CO_2 isothermal adsorption and desorption can be carried out on similar time scales, in principle allowing for simplified process designs and column footprints.

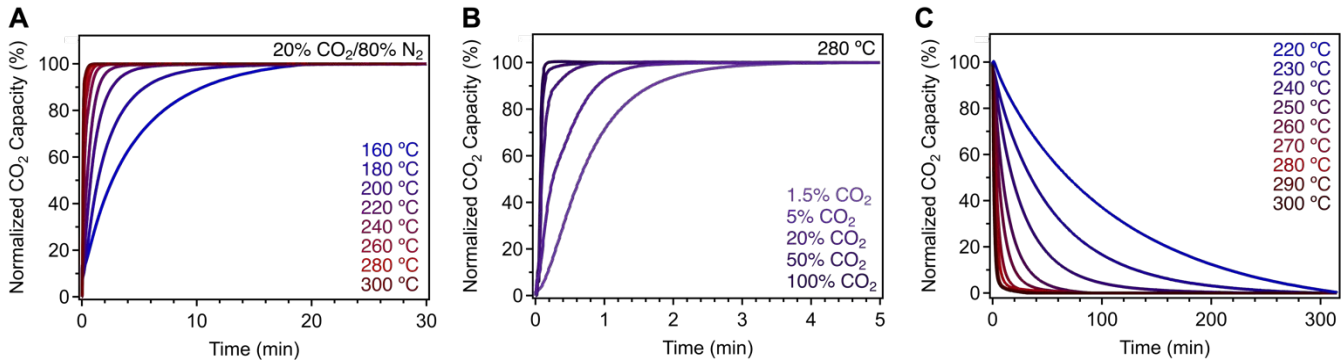

Fig. 4. Kinetic CO_2 adsorption and desorption data. (**A**) Kinetic adsorption profiles collected for ZnH-MFU-4*l* exposed to a flowing 20% CO_2 stream with N_2 balance at temperatures ranging from 160 to 300 °C (see section 2.11.2 of the SM for details). Saturation with CO_2 occurred more rapidly as the temperature of the gas stream was increased. (**B**) Kinetic adsorption profiles collected for ZnH-MFU-4*l* at 280 °C exposed to flowing gas streams with CO_2 concentrations ranging from 1.5% CO_2 (balance N_2) to 100% CO_2. Saturation with CO_2 occurred more rapidly as the concentration of CO_2 was increased. (**C**) Variable-temperature kinetic desorption profiles collected for Zn(OOCH)-MFU-4*l* under flowing N_2 (see section 2.11.4 of the SM for details). All measurements were conducted under a flow rate of 100 mL/min using a thermogravimetric analyzer.

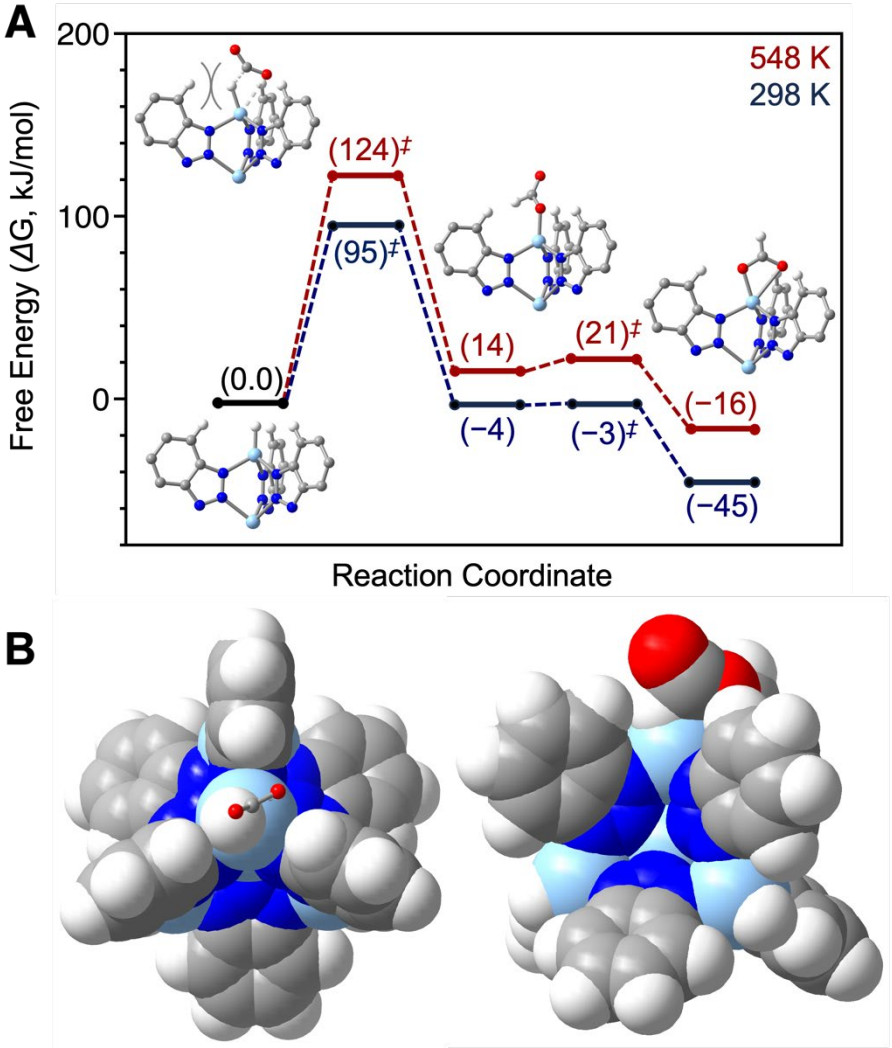

Fig. 5. Calculated Free Energy Landscape for CO_2 Insertion into Zn–H Bond. (**A**) Free energy landscape for the reaction of CO_2 with the model $Zn_5H_4(bta)_6$ cluster to yield $Zn_5(OOCH)_4(bta)_6$ at 25 and 275 °C. The large barrier to CO_2 insertion (95 kJ/mol at 25 °C) is consistent with the absence of CO_2 insertion reactivity at ambient temperature. At 275 °C, there is still a large barrier to CO_2 insertion, but adsorption remains thermodynamically favored (see table S18) and high temperature provides enough thermal energy to overcome this barrier (see section 10 of the SM for computational details). (**B**) Overhead (left) and side-on (right) views of space-filling models illustrating the calculated transition state for CO_2 insertion into the Zn–H bond of $Zn_5H_4(bta)_6$. As the CO_2 approaches the metal center, the hydride ligand is displaced and comes into close contact with a hydrogen of one of the bta^- ligands, shifting from 2.97 Å to 2.42 Å. This unfavorable interaction likely contributes to the large activation barrier for CO_2 insertion.

Outlook

We have shown that the porous framework ZnH-MFU-4*l* reversibly captures large quantities of CO_2 above 200 °C to form Zn(OOCH)-MFU-4*l* and can be regenerated isothermally using vacuum-swing adsorption. The ZnH-MFU-4*l* material is robust to repeated cycling with CO_2 at high temperatures and in the presence of gases such as O_2. This behavior is unprecedented among

porous solids, and these results establish a new direction in porous materials research aimed at the reversible capture of CO_2 at elevated temperatures. Further, these results hint at the enticing prospect of designing MOFs for the high-temperature capture of other industrially relevant gases, which could replace energy-intensive schemes for separations (e.g., cryogenic distillation to separate NH_3 produced via the Haber-Bosch process). Investigations are ongoing in our laboratories to establish new design principles for adsorbents capable of high-temperature capture of other industrially-relevant gases.

Acknowledgments. R.C.R. is supported by the NASA Space Technology Graduate Research Opportunity fellowship. K.M.C. is supported by an Arnold O. Beckman postdoctoral fellowship. M.N.D. is supported by a National Science Foundation Graduate Research Fellowship. We thank Dr. Andrey Yakovenko for technical assistance on PXRD refinement. Certain commercial equipment, instruments, or materials are identified in this document. Such identification does not imply recommendation or endorsement by the National Institute of Standards and Technology, nor does it imply that the products identified are necessarily the best available for the purpose. The views expressed in the article do not necessarily represent the views of the DOE or the U.S. Government. The U.S. Government retains and the publisher, by accepting the article for publication, acknowledges that the U.S. Government retains a nonexclusive, paid-up, irrevocable, worldwide license to publish or reproduce the published form of this work, or allow others to do so, for U.S. Government purposes. This research used resources of the Advanced Photon Source (APS), a DOE Office of Science user facility operated for the DOE Office of Science by Argonne National Laboratory under Contract No. DE-AC02-06CH11357. R.A.K. gratefully acknowledges from the U.S. DOE Office of Energy Efficiency and Renewable Energy (EERE), Hydrogen and Fuel Cell Technologies Office (HFTO) contract no. DE-AC36-8GO28308 to the National Renewable Energy Laboratory (NREL). This research used resources of the National Energy Research Scientific Computing Center (NERSC), a U.S. Department of Energy Office of Science User Facility located at Lawrence Berkeley National Laboratory, operated under Contract No. DE-AC02-05CH11231 using NERSC award BES-ERCAP-0023680. We thank J. L. Peltier, B. E. R. Snyder, and J. Börgel (UC Berkeley) for helpful discussions. We thank T. D. Harris and K. R. Meihaus (UC Berkeley) for editorial assistance.

Funding: This work was supported by the Department of Energy Office of Science, Office of Basic Energy Sciences, under Award DESC0019992.

Author contributions: R.C.R., K.M.C., and J.R.L. formulated and directed the research. R.C.R. and K.M.C. optimized materials, conducted isotherm and isobar measurements, and analyzed data. R.C.R, K.M.C., and M.N.D. conducted and interpreted kinetic measurements. H.K., A.J.H., and J.W.T. assisted in the collected and refinement of single-crystal x-ray diffraction data. H.Z.H.J., R.A.K., S.L.K., Y.W.; K.E.E., Y.Y., J.A.R., and C.M.B. conducted spectroscopic characterization. A.M. and M.H.G. conducted calculations. R.C.R and K.M.C. drafted the manuscript. All authors contributed to revision of the manuscript.

Competing interests: The authors declare the following competing interests: The University of California, Berkeley has applied for a patent on some of the technology discussed herein regarding high-temperature gas capture with porous materials, on which R.C.R., K.M.C., and J.R.L. are listed

as co-inventors. J.R.L. has a financial interest in Mosaic Materials, Inc., a start-up company working to commercialize metal−organic frameworks for gas separations.

Data and materials availability: The supplementary materials contain complete experimental and spectral details for all new compounds reported herein. Crystallographic data have been made available free of charge from the Cambridge Crystallographic Data Centre under deposition numbers 2250026 (ZnEt-MFU-4*l*), 2250025 (Zn(OOCH)-MFU-4*l*), 2250027 (ZnH-MFU-4*l*), and 2166411 (CO_2-derived Zn(OOCH)-MFU-4*l*).

References and Notes

(1) Budinis, S.; Krevor, S.; Mac Dowell, N.; Brandon, N.; Hawkes, A. An Assessment of CCS Costs, Barriers and Potential. *Energy strategy reviews* **2018**, *22*, 61–81.

(2) Masson-Delmotte, V.; Zhai, P.; Pörtner, H.-O.; Roberts, D.; Skea, J.; Shukla, P. R.; Pirani, A.; Moufouma-Okia, W.; Péan, C.; Pidcock, R. Global Warming of 1.5 C. *An IPCC Special Report on the impacts of global warming of* **2018**, *1* (5), 43–50.

(3) International Energy Agency. *Renewable 2021: Analysis and Forecast to 2026*; IEA: Paris, 2021. https://www.iea.org/reports/renewables-2021.

(4) IEA. *World Energy Outlook 2022*; IEA, Paris, France, 2022.

(5) Quadrelli, R.; Peterson, S. The Energy–Climate Challenge: Recent Trends in CO2 Emissions from Fuel Combustion. *Energy Policy* **2007**, *35* (11), 5938–5952. https://doi.org/10.1016/j.enpol.2007.07.001.

(6) Davis, S. J.; Lewis, N. S.; Shaner, M.; Aggarwal, S.; Arent, D.; Azevedo, I. L.; Benson, S. M.; Bradley, T.; Brouwer, J.; Chiang, Y.-M.; Clack, C. T. M.; Cohen, A.; Doig, S.; Edmonds, J.; Fennell, P.; Field, C. B.; Hannegan, B.; Hodge, B.-M.; Hoffert, M. I.; Ingersoll, E.; Jaramillo, P.; Lackner, K. S.; Mach, K. J.; Mastrandrea, M.; Ogden, J.; Peterson, P. F.; Sanchez, D. L.; Sperling, D.; Stagner, J.; Trancik, J. E.; Yang, C.-J.; Caldeira, K. Net-Zero Emissions Energy Systems. *Science* **2018**, *360* (6396), eaas9793. https://doi.org/10.1126/science.aas9793.

(7) Rochelle, G. T. Amine Scrubbing for CO2 Capture. *Science* **2009**, *325* (5948), 1652–1654.

(8) Yu, C.-H.; Huang, C.-H.; Tan, C.-S. A Review of CO2 Capture by Absorption and Adsorption. *Aerosol and Air Quality Research* **2012**, *12* (5), 745–769.

(9) Mazari, S. A.; Ali, B. S.; Jan, B. M.; Saeed, I. M.; Nizamuddin, S. An Overview of Solvent Management and Emissions of Amine-Based CO2 Capture Technology. *International Journal of Greenhouse Gas Control* **2015**, *34*, 129–140.

(10) Rosa, L.; Reimer, J. A.; Went, M. S.; D'Odorico, P. Hydrological Limits to Carbon Capture and Storage. *Nature Sustainability* **2020**, *3* (8), 658–666. https://doi.org/10.1038/s41893-020-0532-7.

(11) Zhai, H.; Rubin, E. S.; Versteeg, P. L. Water Use at Pulverized Coal Power Plants with Postcombustion Carbon Capture and Storage. *Environmental science & technology* **2011**, *45* (6), 2479–2485.

(12) Halliday, C.; Hatton, T. A. The Potential of Molten Metal Oxide Sorbents for Carbon Capture at High Temperature: Conceptual Design. *Applied Energy* **2020**, *280*, 116016. https://doi.org/10.1016/j.apenergy.2020.116016.

(13) Lara, Y.; Martínez, A.; Lisbona, P.; Romeo, L. M. Energy Integration of High and Low Temperature Solid Sorbents for CO2 Capture. *Energy Procedia* **2017**, *114*, 2380–2389. https://doi.org/10.1016/j.egypro.2017.03.1384.

(14) Blamey, J.; Anthony, E. J.; Wang, J.; Fennell, P. S. The Calcium Looping Cycle for Large-Scale CO2 Capture. *Progress in Energy and Combustion Science* **2010**, *36* (2), 260–279. https://doi.org/10.1016/j.pecs.2009.10.001.
(15) Ströhle, J.; Lasheras, A.; Galloy, A.; Epple, B. Simulation of the Carbonate Looping Process for Post-combustion CO2 Capture from a Coal-fired Power Plant. *Chemical Engineering & Technology: Industrial Chemistry-Plant Equipment-Process Engineering-Biotechnology* **2009**, *32* (3), 435–442.
(16) Berstad, D.; Anantharaman, R.; Blom, R.; Jordal, K.; Arstad, B. NGCC Post-Combustion CO2 Capture with Ca/Carbonate Looping: Efficiency Dependency on Sorbent Properties, Capture Unit Performance and Process Configuration. *International Journal of Greenhouse Gas Control* **2014**, *24*, 43–53. https://doi.org/10.1016/j.ijggc.2014.02.015.
(17) Mahajan, S.; Lahtinen, M. Recent Progress in Metal-Organic Frameworks (MOFs) for CO2 Capture at Different Pressures. *Journal of Environmental Chemical Engineering* **2022**, *10* (6), 108930. https://doi.org/10.1016/j.jece.2022.108930.
(18) Siegelman, R. L.; Kim, E. J.; Long, J. R. Porous Materials for Carbon Dioxide Separations. *Nature Materials* **2021**, *20* (8), 1060–1072. https://doi.org/10.1038/s41563-021-01054-8.
(19) Kim, E. J.; Siegelman, R. L.; Jiang, H. Z. H.; Forse, A. C.; Lee, J.-H.; Martell, J. D.; Milner, P. J.; Falkowski, J. M.; Neaton, J. B.; Reimer, J. A.; Weston, S. C.; Long, J. R. Cooperative Carbon Capture and Steam Regeneration with Tetraamine-Appended Metal–Organic Frameworks. *Science* **2020**, *369* (6502), 392–396. https://doi.org/10.1126/science.abb3976.
(20) Drage, T. C.; Snape, C. E.; Stevens, L. A.; Wood, J.; Wang, J.; Cooper, A. I.; Dawson, R.; Guo, X.; Satterley, C.; Irons, R. Materials Challenges for the Development of Solid Sorbents for Post-Combustion Carbon Capture. *Journal of Materials Chemistry* **2012**, *22* (7), 2815–2823.
(21) Sumida, K.; Rogow, D. L.; Mason, J. A.; McDonald, T. M.; Bloch, E. D.; Herm, Z. R.; Bae, T.-H.; Long, J. R. Carbon Dioxide Capture in Metal–Organic Frameworks. *Chem. Rev.* **2012**, *112* (2), 724–781. https://doi.org/10.1021/cr2003272.
(22) Furukawa, H.; Cordova, K. E.; O'Keeffe, M.; Yaghi, O. M. The Chemistry and Applications of Metal-Organic Frameworks. *Science* **2013**, *341* (6149), 1230444.
(23) Martell, J. D.; Milner, P. J.; Siegelman, R. L.; Long, J. R. Kinetics of Cooperative CO2 Adsorption in Diamine-Appended Variants of the Metal–Organic Framework Mg2(Dobpdc). *Chem. Sci.* **2020**, *11* (25), 6457–6471. https://doi.org/10.1039/D0SC01087A.
(24) Looney, A.; Han, R.; Gorrell, I. B.; Cornebise, M.; Yoon, K.; Parkin, G.; Rheingold, A. L. Monomeric Alkyl and Hydride Derivatives of Zinc Supported by Poly(Pyrazoly)Hydroborato Ligation: Synthetic, Structural, and Reactivity Studies. *Organometallics* **1995**, *14* (1), 274–288. https://doi.org/10.1021/om00001a041.
(25) Ritter, F.; Spaniol, T. P.; Douair, I.; Maron, L.; Okuda, J. Molecular Zinc Hydride Cations [ZnH]+: Synthesis, Structure, and CO2 Hydrosilylation Catalysis. *Angewandte Chemie International Edition* **2020**, *59* (51), 23335–23342. https://doi.org/10.1002/anie.202011480.
(26) Sattler, W.; Parkin, G. Synthesis, Structure, and Reactivity of a Mononuclear Organozinc Hydride Complex: Facile Insertion of CO2 into a Zn–H Bond and CO2-Promoted Displacement of Siloxide Ligands. *J. Am. Chem. Soc.* **2011**, *133* (25), 9708–9711. https://doi.org/10.1021/ja2035706.

(27) Kreider-Mueller, A.; Quinlivan, P. J.; Rauch, M.; Owen, J. S.; Parkin, G. Synthesis, Structure and Reactivity of [TmBut]ZnH, a Monomeric Terminal Zinc Hydride Compound in a Sulfur-Rich Coordination Environment: Access to a Heterobimetallic Compound. *Chem. Commun.* **2016**, *52* (11), 2358–2361. https://doi.org/10.1039/C5CC08915H.
(28) Han, R.; Gorrell, I. B.; Looney, A. G.; Parkin, G. Tris(3-Tert-Butylpyrazolyl)Hydroborato Zinc Hydride: Synthesis, Structure and Reactivity of a Monomeric Zinc Hydride Derivative. *J. Chem. Soc., Chem. Commun.* **1991**, No. 10, 717–719. https://doi.org/10.1039/C39910000717.
(29) Denysenko, D.; Grzywa, M.; Jelic, J.; Reuter, K.; Volkmer, D. Scorpionate-Type Coordination in MFU-4l Metal–Organic Frameworks: Small-Molecule Binding and Activation upon the Thermally Activated Formation of Open Metal Sites. *Angewandte Chemie International Edition* **2014**, *53* (23), 5832–5836. https://doi.org/10.1002/anie.201310004.
(30) Denysenko, D.; Grzywa, M.; Tonigold, M.; Streppel, B.; Krkljus, I.; Hirscher, M.; Mugnaioli, E.; Kolb, U.; Hanss, J.; Volkmer, D. Elucidating Gating Effects for Hydrogen Sorption in MFU-4-Type Triazolate-Based Metal–Organic Frameworks Featuring Different Pore Sizes. *Chemistry – A European Journal* **2011**, *17* (6), 1837–1848. https://doi.org/10.1002/chem.201001872.
(31) Röß-Ohlenroth, R.; Bredenkötter, B.; Volkmer, D. Organometallic MFU-4l(Arge) Metal–Organic Frameworks. *Organometallics* **2019**, *38* (18), 3444–3452. https://doi.org/10.1021/acs.organomet.9b00297.
(32) Liao, P.-Q.; Chen, H.; Zhou, D.-D.; Liu, S.-Y.; He, C.-T.; Rui, Z.; Ji, H.; Zhang, J.-P.; Chen, X.-M. Monodentate Hydroxide as a Super Strong yet Reversible Active Site for CO2 Capture from High-Humidity Flue Gas. *Energy Environ. Sci.* **2015**, *8* (3), 1011–1016. https://doi.org/10.1039/C4EE02717E.
(33) McQueen, N.; Woodall, C. M.; Psarras, P.; Wilcox, J. CCS in the Iron and Steel Industry. In *Carbon Capture and Storage*; Reiner, D., Bui, M., Mac Dowell, N., Eds.; The Royal Society of Chemistry, 2019; p 0. https://doi.org/10.1039/9781788012744-00353.
(34) Hills, T. P.; Sceats, M. G.; Fennell, P. S. Applications of CCS in the Cement Industry. In *Carbon Capture and Storage*; Reiner, D., Bui, M., Mac Dowell, N., Eds.; The Royal Society of Chemistry, 2019; p 0. https://doi.org/10.1039/9781788012744-00315.
(35) Mason, J. A.; Sumida, K.; Herm, Z. R.; Krishna, R.; Long, Jeffrey. R. Evaluating Metal–Organic Frameworks for Post-Combustion Carbon Dioxide Capture via Temperature Swing Adsorption. *Energy Environ. Sci.* **2011**, *4* (8), 3030–3040. https://doi.org/10.1039/C1EE01720A.
(36) Lee, A.; Xiao, G.; Xiao, P.; Joshi, K.; Singh, R.; Webley, P. A. High Temperature Adsorption Materials and Their Performance for Pre-Combustion Capture of Carbon Dioxide. *Energy Procedia* **2011**, *4*, 1199–1206. https://doi.org/10.1016/j.egypro.2011.01.174.
(37) Schmieder, P.; Denysenko, D.; Grzywa, M.; Baumgärtner, B.; Senkovska, I.; Kaskel, S.; Sastre, G.; van Wüllen, L.; Volkmer, D. CFA-1: The First Chiral Metal–Organic Framework Containing Kuratowski-Type Secondary Building Units. *Dalton Trans.* **2013**, *42* (30), 10786–10797. https://doi.org/10.1039/C3DT50787D.
(38) Metzger, E. D.; Comito, R. J.; Wu, Z.; Zhang, G.; Dubey, R. C.; Xu, W.; Miller, J. T.; Dincă, M. Highly Selective Heterogeneous Ethylene Dimerization with a Scalable and Chemically Robust MOF Catalyst. *ACS Sustainable Chem. Eng.* **2019**, *7* (7), 6654–6661. https://doi.org/10.1021/acssuschemeng.8b05703.

(39) Booras, G. S.; Smelser, S. C. An Engineering and Economic Evaluation of CO2 Removal from Fossil-Fuel-Fired Power Plants. *Energy* **1991**, *16* (11), 1295–1305. https://doi.org/10.1016/0360-5442(91)90003-5.
(40) Rao, A. B.; Rubin, E. S. Identifying Cost-Effective CO2 Control Levels for Amine-Based CO2 Capture Systems. *Industrial & engineering chemistry research* **2006**, *45* (8), 2421–2429.
(41) Wright, A. M.; Wu, Z.; Zhang, G.; Mancuso, J. L.; Comito, R. J.; Day, R. W.; Hendon, C. H.; Miller, J. T.; Dincă, M. A Structural Mimic of Carbonic Anhydrase in a Metal-Organic Framework. *Chem* **2018**, *4* (12), 2894–2901.
(42) Cai, Z.; Bien, C. E.; Liu, Q.; Wade, C. R. Insights into CO2 Adsorption in M–OH Functionalized MOFs. *Chem. Mater.* **2020**, *32* (10), 4257–4264. https://doi.org/10.1021/acs.chemmater.0c00746.